In Situ Preparation of Sandwich MoO_3/C Hybrid Nanostructures for High-Rate and Ultralong-Life Supercapacitors

Hongmei Ji, Xiaolin Liu, Zhijuan Liu, Bo Yan, Lin Chen, Yafeng Xie, Chao Liu, Wenhua Hou, and Gang Yang**

This work presents a design of sandwich MoO_3/C hybrid nanostructure via calcination of the dodecylamine-intercalated layered α-MoO_3, leading to the in situ production of the interlayered graphene layer. The sample with a high degree of graphitization of graphene layer and more interlayered void region exhibits the most outstanding energy storage performance. The obtained material is capable of delivering a high specific capacitance of 331 F g^{-1} at a current density of 1 A g^{-1} and retained 71% capacitance at 10 A g^{-1}. In addition, nearly no discharge capacity decay between 1000 and 10 000 continuous charge–discharge cycles is observed at a high current density of 10 A g^{-1}, indicating an excellent specific capacitance retention ability. The exceptional rate capability endows the electrode with a high energy density of 41.2 W h kg^{-1} and a high power density of 12.0 kW kg^{-1} simultaneously. The excellent performance is attributed to the sandwich hybrid nanostructure of MoO_3/C with broad ion diffusion pathway, low charge-transfer resistance, and robust structure at high current density for long-time cycling. The present work provides an insight into the fabrication of novel electrode materials with both enhanced rate capability and cyclability for potential use in supercapacitor and other energy storage devices.

1. Introduction

Electrochemical supercapacitors have the advantages of delivering a higher density of power than rechargeable batteries and storing a higher density of energy than conventional electrostatic capacitors.[1] However, to achieve a wide application, a high rate capability and a long cycle life are two of the key challenges for supercapacitors.[2] Supercapacitors are mainly classified as electrical double layer capacitors (EDLCs) and pseudocapacitors. Compared with EDLC, pseudocapacitor has faradic redox reactions between electrode and adsorbed/inserted electrolyte ions, storing an energy 10–100 times that of EDLCs.[3] According to the energy storage mechanisms, more ion-accessible sites and fast ion diffusion are crucial for an electrode material to have a high rate capability and thus be used efficiently no matter whether as an EDLC or a pseudocapacitor. To meet the demands for high performance supercapacitors, researchers reduced the diffusion resistance in the solid phase by decreasing the size and thus shortening the diffusion paths,[4] facilitated the ionic diffusion between solid phase and electrolyte by constructing well-designed morphology or porous structure[5] and even loaded very small quantity of active mass to achieve a high capacitance. These strategies could effectively improve the diffusion and intercalation/deintercalation on the surface/interface of the electrode material, but the low ionic diffusion inside the solid phase is still unsolved essentially because of the closed state of the structure units for most electrode materials.

Transition metal dichalcogenides/oxides with layered structures consisting of van der Waals bonded the inplane 2D crystals, are very attractive materials for charge storage because of their ability to intercalate ions at a wide range of sites.[6] MoS_2 nanowall films with a high density of basal edges were reported to have a large number of accessible "entry" sites whereby intersheet diffusion of ion can occur for faradic reaction to enhance the charge storage capability.[7] However, the faradic process was observable only at very low scan rates due to the very slow ion diffusion process in the interlayers. The mesoporous layered crystalline MoO_3 domains, in which Li^+ ions were inserted into the van der Waals gaps, were synthesized, and exhibited an increased charge-storage capacity compared with the nonporous crystalline MoO_3 or mesoporous amorphous material.[8] It can be anticipated that this kind of layered materials would exhibit more available reaction sites in the interlayers compared with other electrode materials. Nevertheless, controlling the corresponding electrode material as thin film or with a porous structure is necessary due to a small

Dr. H. Ji, Dr. X. Liu, Dr. C. Liu, Prof. W. Hou
Key Laboratory of Mesoscopic Chemistry of MOE
School of Chemistry and Chemical Engineering
Nanjing University
Nanjing 210093, P.R. China
E-mail: whou@nju.edu.cn
Dr. H. Ji, Z. Liu, B. Yan, L. Chen, Y. Xie, Prof. G. Yang
Jiangsu Laboratory of Advanced Functional Materials
Department of Chemistry, Changshu Institute of Technology
Changshu 215500, P.R. China
E-mail: gyang@cslg.edu.cn

DOI: 10.1002/adfm.201404378

interlayer distance and a high charge-transfer resistance in the bulk materials. Another interesting attempt is to exfoliate the bulk layered compounds into few-layered 2D nanosheets and assembled with graphene layer-by-layer to lower the charge-transfer resistance and thus obtain a high capacitance. Several composites have been designed for supercapacitor application, such as $VOPO_4$/graphene hybrid film,[9] ultrathin MnO_2/graphene hybrid nanostructure,[10] β-$Ni(OH)_2$/graphene nanohybrids,[11] and Co–Al hydroxide nanosheets/graphene multilayer films.[12] This kind of hybrid structure stacked layer-by-layer can tailor the distance between each sheet and open up the interlayer space to allow for more electrolyte ions to penetrate efficiently into the hybrid film during charging/discharging processes. Meanwhile, the introduction of graphene layer could make the whole composite with a good electronic conductivity as the poor electrical conductivity of transition metal oxides severely affects their specific capacitance, especially the high rate capacity. Hence, improving the electrical conductivity of electrode materials is as important as lowering the ion diffusion resistance for obtaining a high energy storage performance.

In general, the layer-by-layer stacked structure has the advantage of obtaining a better electrochemical performance compared with those large-size electrode materials mechanically mixed with the conductive additives. However, research on this aspect is at the initial stage because of the following reasons: (1) The exfoliation process of the bulk layered compounds is complicated and should be strictly controlled.[13] Moreover, the yield of monolayered, or few-layered 2D nanosheets is very low (usually several mg mL^{-1}),[14] meaning hard for large scale application. (2) In the liquid-phase exfoliation, certain organic solvent with an appropriate surface energy was used to remove the drive force for the reaggregation of exfoliated nanosheets in recently reported strategies.[15] Sometimes, surfactant or polymer was needed to provide nanosheets with an electrostatical or a sterical stability.[16] These additives are expensive, toxic, and difficult to remove. Besides, the remained additives would influence the physical and chemical properties of the obtained nanosheets for their further device application.[17] (3) In general, in turn vacuum filtration was often used to prepare hybrid nanostructure/film and this technology is hard to completely realize the layer-by-layer combination. In addition, the pure monolayered 2D sheets are few and they would be restacked and aggregated more or less, leading to the reconstruction and inhomogeneous distribution of constituents in the products.[9–11]

Herein, using layered α-MoO_3 as the starting material, a facile and controllable method was used to in situ produce a unique sandwich MoO_3/C hybrid nanostructure assembled of α-MoO_3 and graphene at a molecular level. The dodecylamine (DDA) was used as an intercalating agent to result a DDA-intercalated MoO_3 nanocomposite (MoO_3/DDA). The intercalated DDA was then in situ carbonized to achieve the assembly of MoO_3 and graphene layers stacked alternatively. As electrode material for supercapacitor, this kind of sandwich hybrid nanostructure had the advantages of more ion-accessible sites, rapid ion/electron transmission, and excellent structure stability, giving rise to outstanding rate capability and cycling stability.

2. Results and Discussion

2.1. The Structure and Morphology of the Hybrid Nanostructures

Briefly, the fabrication process of sandwich MoO_3/C hybrid nanostructures for high-performance supercapacitor is schematically shown in **Figure 1**a. Due to the alcoholysis of $CH_3(CH_2)_{11}NH_2$ and the requirement of electric neutrality, $CH_3(CH_2)_{11}NH_3^+$ ions were intercalated into the interlayers of MoO_3, which was proved by XRD results. As shown in Figure 1 b, the commercial MoO_3 has the typical intense reflections of layered structure (JCPDS: 35-0609), with an interlayer spacing d_{010} of 0.69 nm ($2\theta = 12.86°$). As for MoO_3/DDA, five sharp (0k0) peaks at low angles (2°–15°) overwhelmingly dominate the diffraction pattern. Moreover, the interlayer spacing d_{010} of MoO_3 was greatly increased to 3.13 nm ($2\theta = 2.82°$), indicating the successful intercalation of DDA into MoO_3. Since the length of DDA molecule is ≈1.78 nm,[18] it can be estimated that a bilayer arrangement of DDA molecules was formed in the interlayers of MoO_3 (see Figure 1a).

Upon calcination of MoO_3/DDA, the interlayered DDA molecules would be in situ carbonized. As shown in Figure 1a, after calcination at 400 and 600 °C, the intercalation structures at a molecular level are still remained, being composed of MoO_3 and graphene layers. Due to the conversion of DDA to carbon and the simultaneous removal of small molecules, the (010) reflection peak was largely weakened and shifted to $2\theta = 4.15°$ and 4.85°, respectively (inset of Figure 1b). It can be calculated that the interlayer spacings of the resulted MoO_3/C-400 and MoO_3/C-600 are 2.17 and 1.80 nm, respectively. However, as the carbonization temperature was further raised up to 750 °C, the characteristic (010) diffraction peak disappeared and new diffraction peaks referred to Mo_2C (marked with triangle) and MoO_2 (labeled with circle) appeared in MoO_3/C-750, indicating that the ordered intercalation structure was collapsed and new crystal phases were formed due to the reaction of the interlayered carbon with molybdenum oxide layer. No significantly characteristic peaks of MoO_3 in MoO_3/DDA, MoO_3/C-400, MoO_3/C-600, and MoO_3/C-750 could be observed in XRD patterns, the possible reason might be the destruction of the long range order of MoO_3 bulk crystals due to the intercalation of guest molecules such as DDA and carbon.

As shown in SEM images (**Figure 2**), the commercial MoO_3 is full of rather uniform plates with a micrometer-size. MoO_3/DDA, MoO_3/C-400, and MoO_3/C-600 are all comprised of lamellar plates, but the plate thickness is gradually decreased. This suggests that the intercalated guests shrink and become compact with the increased annealing temperature, which is in accordance with the interlayer spacing calculated from XRD patterns. In addition, the elemental mapping images also confirm the uniform distribution of C, Mo, and O in MoO_3/C-400 and MoO_3/C-600 (Figure S1, Supporting Information and Figure 2f). By comparison, the SEM image (Figure 2e) of MoO_3/C-750 presents that the plates are not smooth and flat, and the inset magnified image shows that the plates appeared in MoO_3/C-400 and MoO_3/C-600 are split off and many thinner slices are formed with some small particles of Mo_2C, MoO_2, and carbon discontinuously dispersed on the surface.

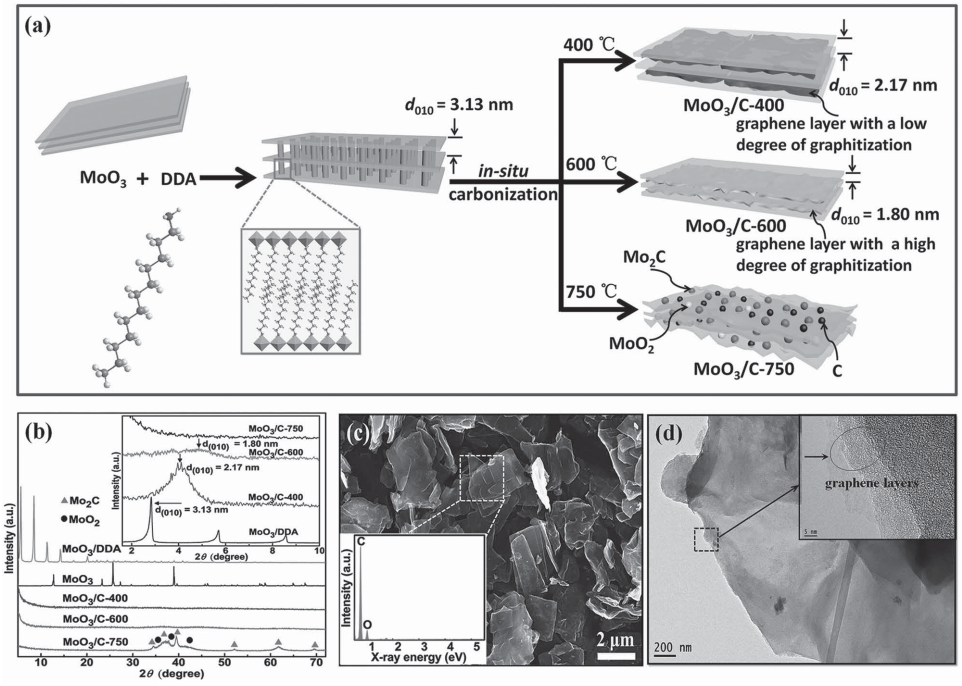

Figure 1. a) Schematic illustration for the fabrication of sandwich MoO_3/C hybrid nanostructures. b) Large and small angle (inset) XRD patterns of α-MoO_3, MoO_3/DDA, MoO_3/C-400, MoO_3/C-600, and MoO_3/C-750, respectively. c) SEM and d) TEM images of the interlayered graphene obtained by dissolving MoO_3/C-600 in 2 mol L^{-1} NaOH solution to eliminate host MoO_3 layers; the inset of (c,d) are EDX spectrum and HRTEM image of the selected region, respectively.

Since the sandwich MoO_3/C hybrid nanostructures were synthesized by the in situ carbonization of the intercalated organic agent DDA, the carbon structure formed in the interlayers needs to be clearly investigated. To completely remove MoO_3 host layers, the typical sample MoO_3/C-600 was selected as an example to be immersed in 2 mol L^{-1} NaOH solution with continually stirring for 24 h and then filtered and washed with deionized water and ethanol for three times. The energy-dispersive X-ray (EDX) analysis (inset of Figure 1c) demonstrated that MoO_3 host layers were totally removed and only carbon left. The morphology of lamellar plates is largely retained (Figure 1c) and the dimension of these plates is smaller than that of MoO_3 layers. As shown in Figure 1d, the intercalated carbon layers are composed of few-layered graphene with a large area.

Raman spectra were recorded to further study the nature of graphene formed in the samples. As shown in Figure S2a, Supporting Information, the characteristic signals located at around 1350 and 1580 cm^{-1} are attributed to D-band from disordered carbon and G-band from graphene, respectively.[19] It is noted that the intensity ratio of these two bands (I_D/I_G)

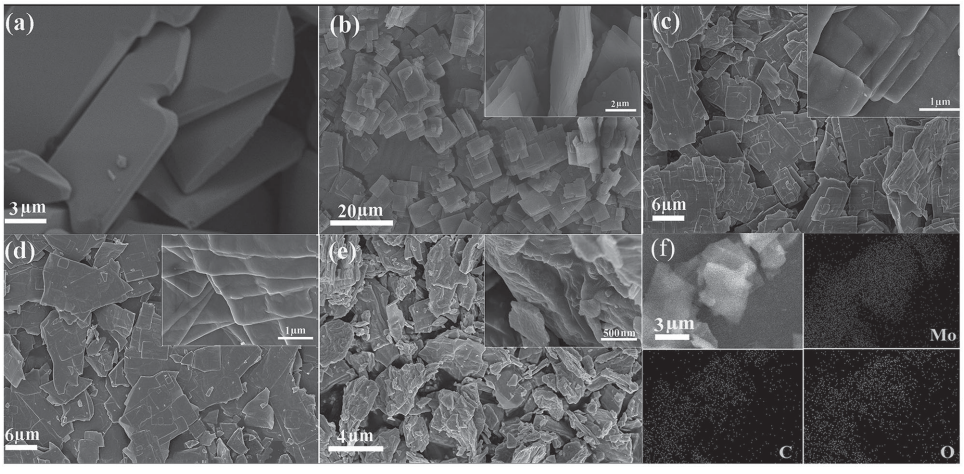

Figure 2. SEM images of a) α-MoO_3, b) MoO_3/DDA, c) MoO_3/C-400, d) MoO_3/C-600, and e) MoO_3/C-750 (insets are enlarged images). f) Elemental mapping images of MoO_3/C-600.

is lower in MoO_3/C-600 and MoO_3/C-750 than that in MoO_3/C-400, reflecting a high degree of graphitization in the obtained products at a relatively high carbonization temperature. This result was also confirmed by the elemental analysis. As listed in Table S1, Supporting Information, the oxygen content and C/H molar ratio were determined as 31.0 wt% and 10.0 in MoO_3/C-400 and 25.8 wt% and 22.3 in MoO_3/C-600, respectively. The carbonization at a higher temperature removed more noncarbon constituents and made the intercalation structure more compact. Accordingly, the oxygen content would be sharply declined and the molar ratios of C/N and C/H increased with the annealing temperature. A high degree of graphitization can improve the electronic conductivity of the products, being favorable for obtaining satisfied electrochemical performance.

Figure S2b, Supporting Information, shows N_2 adsorption/desorption isotherms and the corresponding pore size distribution curves of MoO_3/C-400, MoO_3/C-600, and MoO_3/C-750, respectively. All three samples have a porous structure and a large Brunauer–Emmett–Teller (BET) specific surface area. The BET specific surface areas of MoO_3/C-400, MoO_3/C-600, and MoO_3/C-750 are 122, 129, and 130 $m^2\ g^{-1}$, respectively. By comparison, MoO_3/C-600 demonstrates a more uniform bimodal pore size distribution. The porous structure and a large specific surface area would be beneficial for the charge storage of the electrode materials.

A high-resolution X-ray photoelectron spectroscopy (XPS) measurement was carried out in order to investigate the chemical composition and valence states of Mo and C. **Figure 3**a–c show XPS spectra of Mo 3d region for MoO_3/C-400, MoO_3/C-600, and MoO_3/C-750. For MoO_3/C-400 and MoO_3/C-600, the peaks at 232.2 and 235.1 eV are attributed to $3d_{5/2}$ and $3d_{3/2}$ of Mo^{6+}, respectively. The low energy peak at 229.4 eV can be assigned to Mo^{4+} $3d_{5/2}$, due to the partial reduction of Mo^{6+} occurred in the carbonization process. The amount of Mo^{4+} is very low in these two samples and most of Mo species exists as Mo^{6+} (Table S2, Supporting Information). By comparison, the amount of Mo^{4+} is obviously increased in MoO_3/C-750, indicating that the reduction of Mo^{6+} is relatively easy at a high temperature and most Mo^{6+} species are reduced to Mo^{5+}. Correspondingly, the peak position is shifted from 232.2 (Mo^{6+} $3d_{5/2}$) to 231.6 eV (Mo^{5+} $3d_{5/2}$) (Figure 3c). In addition, a new energy peak of Mo^{2+} ($3d_{5/2}$) appears at 227.6 eV due to the formation of a new phase Mo_2C (see XRD in Figure 1b).

Figure 3d–f show XPS spectra of C 1s region for MoO_3/C-400, MoO_3/C-600, and MoO_3/C-750. The energy peak at 283.9 eV is attributed to C-H, while that at 284.8 eV can be assigned to the intercalated carbon.[20] As listed in Table S3, Supporting Information, the amount of C–H was decreased from 62.1% to 47.1% as the carbonization temperature was increased from 400 to 600 °C. Meanwhile, the content of intercalated carbon was increased from 21.9% in MoO_3/C-400 to 35.8% in MoO_3/C-600. Because the intercalated carbon further reacted with MoO_3 host layers and the layered structure was destroyed, the content of intercalated carbon in MoO_3/C-750 is decreased compared with that in MoO_3/C-600.

In view of the resulted sandwich, MoO_3/C hybrid composite could be an ideal structure for fast diffusion of H^+ ions into the interlayer region for the reduction of metal ions to store the charge, cyclic voltammetry (CV), galvanostatic charge–discharge, and impedance measurements were performed with a three-electrode cell in 1 M H_2SO_4 electrolyte to evaluate the electrochemical and electric performance of MoO_3/C-400, MoO_3/C-600, and MoO_3/C-750.

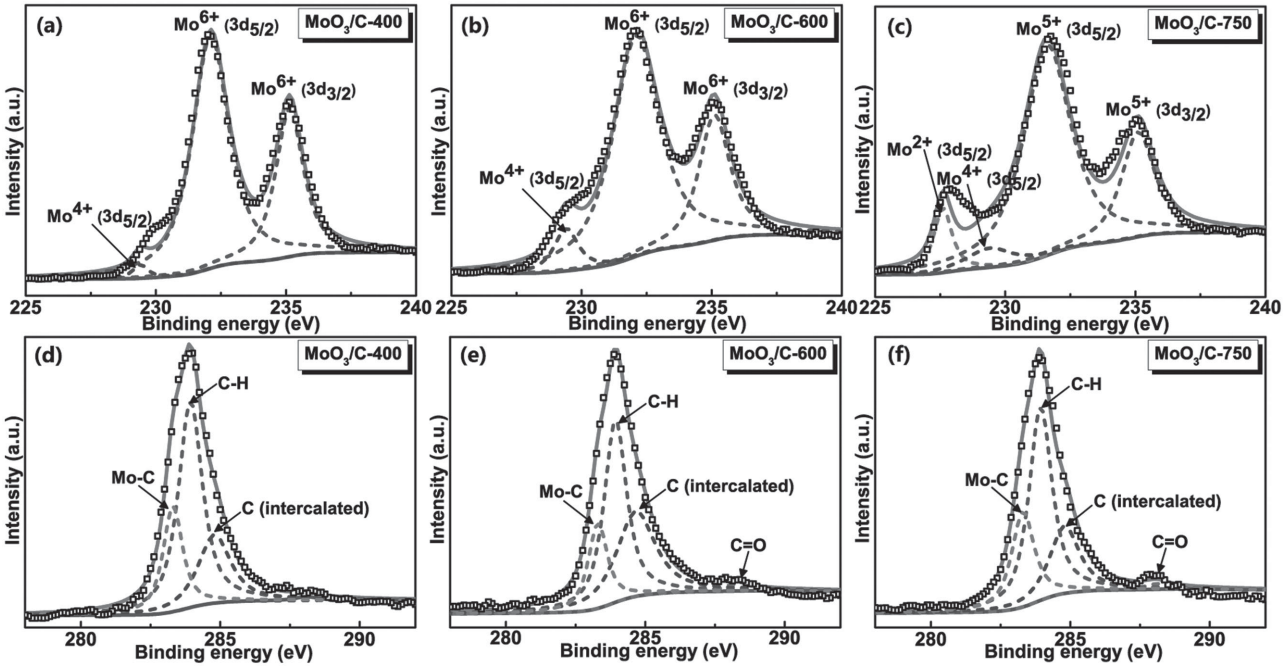

Figure 3. XPS patterns of a,d) MoO_3/C-400, b,e) MoO_3/C-600, and c,f) MoO_3/C-750 in the Mo 3d and C 1s regions, respectively.

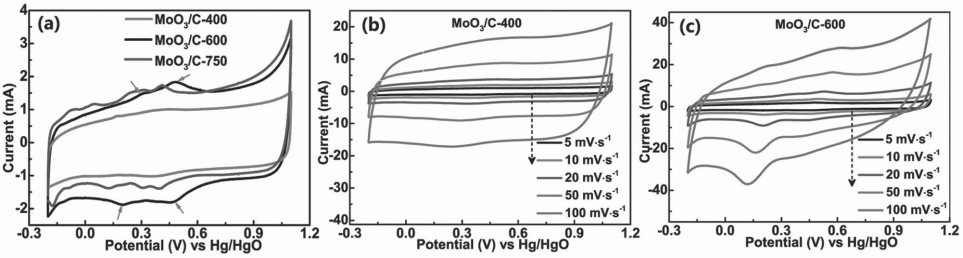

Figure 4. Cyclic voltammogram curves of a) MoO_3/C-400, MoO_3/C-600, and MoO_3/C-750 at a scan rate of 5 mV s^{-1}, b) MoO_3/C-400, and c) MoO_3/C-600 electrodes at different scan rates.

2.2. The Electrochemical Performances of the Hybrid Nanostructures

Figure 4a shows CV curves at a scan rate of 5 mV s^{-1} for MoO_3/C-400, MoO_3/C-600, and MoO_3/C-750. The CV loop area of MoO_3/C-400 is the smallest. In addition, redox peaks are observed both in MoO_3/C-600 and MoO_3/C-750, representing the typical behavior of pseudocapacitor originating from faradic reaction. Two couples of redox peaks in MoO_3/C-600 can be attributed to the intercalation/extraction of H^+ ions into/out of α-MoO_3 interlayers and the simultaneous reduction/oxidation of Mo^{6+} ions as follows[21]

$$x\mathrm{H}^+ + x\mathrm{e}^- + \mathrm{MoO_3} \underset{\text{discharge}}{\overset{\text{charge}}{\rightleftharpoons}} \mathrm{H}_x\mathrm{MoO_3}$$

The CV curve for MoO_3/C-400 presents an approximately rectangular shape without any obvious redox peaks, indicating a typical electrical double-layer capacitance feature at a scan rate of 5 mV s^{-1}. When the potential sweep rate is increased from 5 to 100 mV s^{-1}, the CV curves of MoO_3/C-400 (Figure 4b) remain symmetric and rectangular-like shape except the increased current, meaning a good rate capability because of the facilitated diffusion of H^+ into hybrid nanostructure.[22] In contrast, the CV curve of the commercial MoO_3 presents an obvious deviation when the scan rate is increased up to 100 mV s^{-1} (Figure S3a, Supporting Information), indicating a poor rate capability due to the high internal resistance of the electrode.[23] The comparative result indicates that the layered hybrid structure of MoO_3/C-400 is beneficial for the diffusion of H^+ ions into the interlayers for a double-layer charge storage.

MoO_3/C-600 and MoO_3/C-750 also have the fast H^+ diffusion inside the electrodes and ideal faradic and nonfaradic capacitive behavior, because the peak current is proportional to the scan rate (see Figure 4c and Figure S3b, Supporting Information). Unlike MoO_3/C-400, the pseudocapacitance occurs in MoO_3/C-600 due to more void regions accessible for H^+ ions and its higher electronic conductivity for fast electron transport in the interlayers. It is also supported by the fact that the obvious redox peak appears around 0.14 V, but this redox reaction is partially irreversible due to the structural deformation of α-MoO_3 host layers during the quick intercalation of H^+ for faradic reaction. However, due to the unique sandwich hybrid structure, the formed graphene between α-MoO_3 layers are stable and could act as the buffer to bear the structure change of host materials, making the electrode with a good cycling performance even in a fast charge–discharge process.

Figure 5a shows the charge–discharge curves of MoO_3, MoO_3/DDA, MoO_3/C-400, MoO_3/C-600, and MoO_3/C-750 electrodes collected at a current density of 2 A g^{-1}. Unlike a double-layer capacitance for MoO_3, MoO_3/DDA, and MoO_3/C-400, both MoO_3/C-600 and MoO_3/C-750 showed a slight curvature, indicating the representative pseudocapacitance behavior. This behavior made a great contribution to the high discharge capability of these two samples. Moreover, it can be observed that both MoO_3 and MoO_3/DDA have a limited charge–discharge duration compared with MoO_3/C nanohybrid electrode materials as the ion insertion is limited to the outer surface of electrodes due to the high internal resistance of the bulk structure and DDA-intercalated layered structure.

As shown in Figure 5b,c, MoO_3/C-400, MoO_3/C-600, and MoO_3/C-750 all have a good discharge capability at current rates of 1, 2, 4, 8, and 10 A g^{-1}. According to the above CV results, MoO_3/C-400 mainly delivers a double-layer capacitance, showing a relative lower capacity compared with MoO_3/C-600 and MoO_3/C-750. The specific capacitance of MoO_3/C-400 is 137, 122, 115, 111, and 110 F g^{-1} at 1, 2, 4, 8, and 10 A g^{-1}, showing a ≈81% retention even at 10 A g^{-1} compared to that at 1 A g^{-1}. For MoO_3/C-750 without an alternatively stacked layered structure, it consists of distorted molybdenum oxide 2D flakes coated with MoO_2, Mo_2C, and C particles. The coated C and Mo_2C are beneficial for the electronic conductivity of the electrode material and may also act as active sites for the reversible adsorption/desorption of ions and faradic reaction. Hence, MoO_3/C-750 electrode has a relative higher specific capacitance of 259, 217, 183, 170, and 169 F g^{-1} at 1, 2, 4, 8, and 10 A g^{-1}, respectively, remaining 65% capacity from 1 to 10 A g^{-1}.

Among three samples, MoO_3/C-600 shows the best specific capacitance of 331, 295, 270, 242, and 234 F g^{-1} at 1, 2, 4, 8, and 10 A g^{-1} and a capacity retention of 71% from 1 to 10 A g^{-1}. This result is better than that in the current reports about MoO_3 based electrodes for aqueous supercapacitors.[22a,22c,24] Furthermore, when the current density was turned back to 1 A g^{-1}, about 98.4% of the initial capacity was recovered, better than that of MoO_3/C-400 (94.7%) and MoO_3/C-750 (96.7%). Moreover, as shown in inset of Figure 5c, the IR drop for MoO_3/C-600 is lower compared to the published values, such as H_xMoO_3(0.07 V, 0.5 A g^{-1}), MoO_3 (0.33 V, 0.5 A g^{-1}), and MoO_3/PPy (0.025 V, 0.67 A g^{-1}),[22a,24d] further indicating that the electrode with an elaborately designed hybrid structure has a high electrical conductivity even at a high scan rate.

Figure 5d shows the long-life cycling performance of three samples at a high current density of 10 A g^{-1}. Both MoO_3/

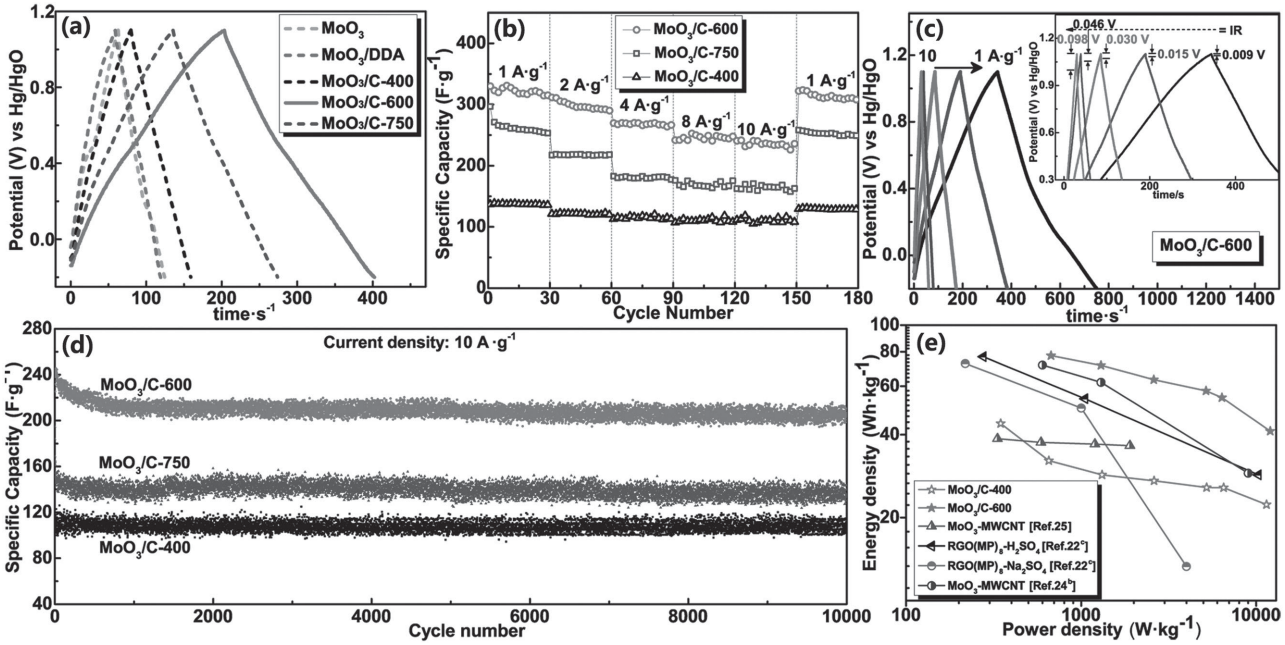

Figure 5. Electrochemical characteristics: a) Charge–discharge profiles at a current density of 2 A g^{-1} in a potential range of –0.2 to 1.1 V. b) Rate performance of MoO_3/C-400, MoO_3/C-600, and MoO_3/C-750 electrodes, respectively. c) Charge–discharge profiles of MoO_3/C-600 electrode at different current densities (inset is the enlarged view of the curves in the relative high voltage). d) Ultralong-life cycling performance of MoO_3/C-400, MoO_3/C-600, and MoO_3/C-750 electrodes at a high current density of 10 A g^{-1}. e) Ragone chart of MoO_3/C-400, MoO_3/C-600 electrodes, and other previously reported data.

C-400 and MoO_3/C-750 electrodes exhibit an initial discharge capacity of 109 ± 9 and 163±8 F g^{-1}, respectively. By comparison, MoO_3/C-600 delivers a remarkably enhanced initial capacitance of 232 ± 10 F g^{-1} and remains more than 87.9% of the initial capacitance after 10 000 cycles. The graphene layers have a good flexibility between host α-MoO_3 layers and resist the change of structure and mechanical stress during the charge–discharge process.

To evaluate the relationship between energy density and power density of the samples, a Ragone plot of energy density versus power density for MoO_3/C-400 and MoO_3/C-600 is shown in Figure 5e. The maximum energy density reached 77.4 W h kg^{-1} for MoO_3/C-600 with a reasonable power density of 0.672 kW kg^{-1}. At a power density of 5.16 kW kg^{-1}, the corresponding energy density was 57.7 W h kg^{-1}. Moreover, the maximum power density of MoO_3/C-600 approached to 12.0 kW kg^{-1} with an energy density of 41.2 W h kg^{-1}, which is notably higher than that of MoO_3/C-400 (11.5 kW kg^{-1}, 22.3 W h kg^{-1}). Overall, MoO_3/C-600 electrode shows an outstanding performance of high-energy density (41.2 W h kg^{-1}) and high-power density (≈12.0 kW kg^{-1}) simultaneously, which is better than those previous results for all MoO_3-based electrodes and meets the performance demands for practical power applications.[22c,24b,25]

Electrochemical impedance spectra (EIS) and the corresponding representation of H^+ ions and electron migration paths inside sandwich MoO_3/graphene hybrid composite during the charge–discharge process are shown in **Figure 6** to

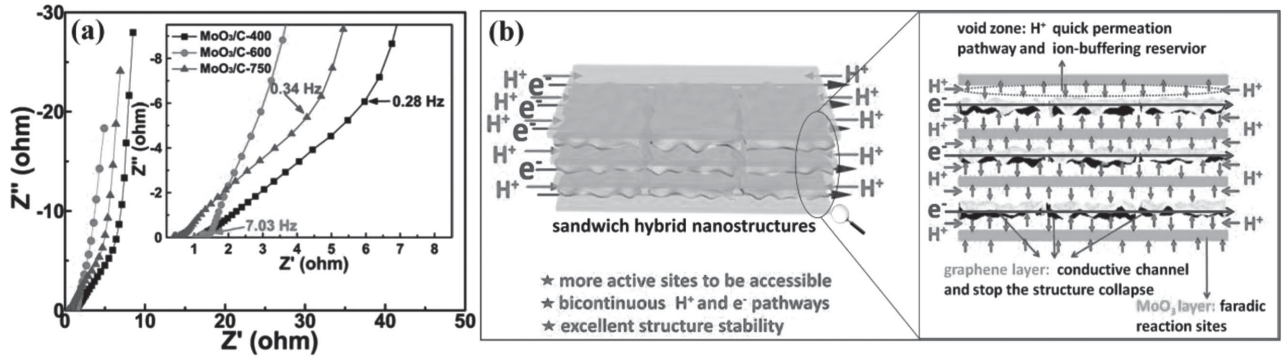

Figure 6. a) Nyquist plots of MoO_3/C-400, MoO_3/C-600, and MoO_3/C-750 electrodes (inset is the high-frequency region of Nyquist plot). b) A representation shows the bicontinuous paths for H^+ ions and fast electron migration inside sandwich MoO_3/graphene hybrid nanocomposite.

reveal the reason for enhanced electrochemical performance of MoO_3/C-600. Figure 6a shows Nyquist plots of MoO_3/C-400, MoO_3/C-600, and MoO_3/C-750 electrodes. At high frequency, the intersection point on the real axis represents equivalent series resistance (ESR, R_s) of the sample. A higher ESR value indicates a lower electrical conductivity of the sample and vice versa. The corresponding ESR value is very low, being 1.71, 0.89, and 0.43 Ω for MoO_3/C-400, MoO_3/C-600, and MoO_3/C-750, respectively (see inset in Figure 6a). By comparison, MoO_3/C-600 has a slightly higher resistance than MoO_3/C-750, which is attributed to the formation of Mo_2C and more oxygen vacancies from a deep reduction of molybdenum oxide in MoO_3/C-750.[26] At the low frequency region, the linear part in the impedance plots is corresponding to Warburg impedance *W*, which is described as a diffusive resistance of H^+ inside molybdenum oxide electrode. The Warburg slope of MoO_3/C-600 is higher than those of MoO_3/C-400 and MoO_3/C-750, further indicating a faster ion diffusion in MoO_3/C-600 electrode due to the fact that it simultaneously has an ordered intercalation structure and a more uniform pore size distribution. The middle frequency line indicates the migration rate of ions from electrolyte to electrode. The crossing of middle-frequency line and low-frequency line defines the "knee frequency,"[27] which was found around 7.03 Hz for MoO_3/C-600 electrode material. The value is much higher than those of MoO_3/C-400 (≈0.28 Hz) and MoO_3/C-750 (≈0.34 Hz). It suggests that MoO_3/C-600 electrode material exhibits a much lower interfacial impedance between electrolyte and electrode than the other electrode materials.

2.3. Charge–Discharge Mechanism of the Hybrid Nanostructures

On the basis of the above results, the superior high-rate and long cycling performance of MoO_3/C-600 is attributed to the advantages of graphene layers with a high degree of graphitization intercalated into layered MoO_3 host layers. As illustrated in Figure 6b, these advantages can be summarized as follows. First, the graphene in situ formed in the interlayers makes more structure units of MoO_3 exposed and accessible for adsorption/desorption of charges and then for faradic reactions. Second, the expanded interlayer spacing facilitates a quicker permeation process of electrolytes. Moreover, the interlayered void region can also be used as the "ion-buffering reservoir," reducing the diffusion distance of H^+ to the layered matrix.[28] Third, the graphene layers offer a well interconnectivity between MoO_3 layers, severing dual functions as both conductive channels and active interface centers for an electrochemical double layer capacitance. The above three factors endow MoO_3/graphene hybrid structure with many accessible active sites, quick permeation of H^+ ions, and good electron transport in the interlayers, resulting in the excellent rate capability. Finally, the interlayered graphene layers can accommodate the strain release and prohibit the possible structural collapse arising from high rate insertion/extraction of H^+ into/from MoO_3 layers, resulting in a long-term cycling performance even at a high current density.

3. Conclusion

In summary, the present work demonstrates a convenient, cost-effective, and potentially scalable technique for synthesizing sandwich MoO_3/graphene hybrid nanostructure. Such a novel hybrid architecture provides not only the enlarged interlayer spacing but also the improved electronic conductivity due to the in situ formation of interlayered graphene. These characters are conveniently for the electrolyte penetration and H^+ diffusion to the interlayered regions for faradic reaction as well as electrostatically adsorption for an electric double-layer capacitance. Meanwhile, the flexibility of the interlayered graphene layers can make the hybrid structure stable and resist the strain release during the prolonged cycling process. These advantages lead to the excellent rate capability and ultralong-life cycling stability of the resulted material. The present work offers a new insight for fabricating effective electrode materials used in the energy storage devices with a desirable high-performance. It is further suggested that a high energy density can be obtained without the expense of power density for the fabricated electrode material with unique sandwich structure.

4. Experimental Section

Materials Preparation: First, the intercalation of DDA into layered host MoO_3 was carried out according to the previous literature.[29] The mixture including MoO_3 (1.4 mmol), DDA (7 mmol), and anhydrous ethanol (20 mL) was refluxed at 70 °C for 96 h. Thereafter, the system was permitted to cool down to the room temperature. The white precipitate was finally collected by filtration and washed several times with anhydrous ethanol and dried in vacuum at 60 °C for 10 h. The obtained intercalation sample (MoO_3/DDA) was then calcined in N_2 (g) at 400, 600, and 750 °C, and the resulted products at three different carbonization temperatures were correspondingly named as MoO_3/C-400, MoO_3/C-600, and MoO_3/C-750, respectively.

Structural and Morphology Characterization: The structure and phase purity of the products were examined by XRD on a Philip-X'Pert X-ray diffractometer equipped with a CuKα radiation source (λ = 1.5418 Å). The general morphologies of the as-synthesized products were characterized by scanning electron microscopy (SEM, JEOL JEM-6300F). Transmission electron microscopy (TEM) and high-resolution transmission electron microscopy (HRTEM) images were obtained by using a JEOL JEM-200CX microscope operating at an accelerating voltage of 200 kV. XPS analysis was carried out on an UlVAC-PHI PHI 5000 VersaProbe spectrometer. The amounts of C, H, O, and N elements were measured with a Vario EL III elemental analyser (Elementar, Germany). Raman spectra were recorded on a French JY LabRam-1B (λ_{ex} = 632.8 nm) spectrometer. N_2 adsorption/desorption isotherms were measured by Micromeritics ASAP 2010 with N_2 as an absorbate at 77 K. Before measurements, all samples were degassed at 300 °C for 6 h. The specific surface area was obtained by the BET equation and the pore size distribution was estimated from the desorption of N_2 isotherms by the Barret–Joyner–Halenda (BJH) method.

Electrochemical Measurements: The working electrode was a mixture of 80 wt% as-synthesized sample, 10 wt% acetylene black, and 10 wt% polyvinylidene difluoride (PVDF) in the presence of *N*-methyl pyrrolidinone (NMP). After being stirred overnight, the slurry was pasted onto a graphite sheet. The working area of the electrode was set as 1 cm × 1 cm and the mass loading of the electrode materials was controlled around 1.5 mg. The thickness of the electrode materials was around 25 μm and made by a doctor blade. The electrode was dried at 120 °C under vacuum for 10 h. The capacitance was measured using a

standard three electrode cell, containing a platinum sheet as a counter electrode, a saturated calomel electrode as a reference electrode, and the as-synthesized product as the working electrode. An aqueous solution containing 1 M H_2SO_4 was used as the electrolyte. The supercapacitor performance was evaluated by CV and galvanostatic charge–discharge techniques within the voltage range of –0.2 to 1.1 V. Different sweep rates (5, 10, 20, 50, 100 mV s^{-1}) and constant current densities (1–10 A g^{-1}) were employed. CV was conducted using a RST3100 electrochemical workstation (Suzhou, China). The galvanostatic charge and discharge experiments were carried out at room temperature using a LAND CT2001A battery testing system (Wuhan, China). EIS measurements were also conducted using a PARSTAT2273 electrochemical workstation (Princeton Applied Research, USA), where the amplitude of the input ac signal was kept at 5 mV and the frequency range was set between 10^{-2} and 10^5 Hz.

Supporting Information

Supporting Information is available from the Wiley Online Library or from the author.

Acknowledgements

The authors greatly appreciate the financial support of Specialized Research Fund for the Doctoral Program of Higher Education (SRFDP, 20130091110010), Natural Science Foundation of Jiangsu Province (BK2011438), National Science Fund for Talent Training in Basic Science (No. J1103310), National Basic Research Program (973 Project) (No. 2009CB623504), and the Modern Analysis Center of Nanjing University. This work was also supported by a Project Funded by the Priority Academic Program Development of Jiangsu Higher Education Institutions. Thanks also go to Prof. Xizhang Wang and Dr. Jin Zhao for their assistance in BET specific surface area and pore size distribution measurement.

Received: December 10, 2014
Revised: January 19, 2015
Published online: February 16, 2015

[1] a) M. Winter, R. J. Brodd, *Chem. Rev.* **2004**, *104*, 4245; b) P. Simon, Y. Gogotsi, *Nat. Mater.* **2008**, *7*, 845; c) A. S. Aricò, P. Bruce, B. Scrosati, J.-M. Tarascon, W. V. Schalkwijk, *Nat. Mater.* **2005**, *4*, 366; d) J. R. Miller, P. Simon, *Science* **2008**, *321*, 651.

[2] a) L. L. Zhang, X. S. Zhao, *Chem. Soc. Rev.* **2009**, *38*, 2520; b) W. F. Wei, X. W. Cui, W. X. Chen, D. G. Ivey, *Chem. Soc. Rev.* **2011**, *40*, 1697.

[3] a) B. E. Conway, V. Birss, J. Wojtowicz, *J. Power Sources* **1997**, *66*, 1; b) M. Jayalakshmi, K. Balasubramanian, *Int. J. Electrochem. Sci.* **2008**, *3*, 1196.

[4] a) W. Sugimoto, H. Iwata, Y. Yasunaga, Y. Murakami, Y. Takasu, *Angew. Chem.* **2003**, *115*, 4226; b) L. Mai, H. Li, Y. Zhao, L. Xu, X. Xu, Y. Luo, Z. Zhang, W. Ke, C. Niu, Q. Zhang, *Sci. Rep.* **2013**, *3*, 1; c) C. C. Hu, K. H. Chan, M. C. Lin, Y. T. Wu, *Nano Lett.* **2006**, *6*, 2690; d) R. Liu, S. B. Lee, *J. Am. Chem. Soc.* **2007**, *130*, 2942.

[5] a) U. Nithiyanantham, A. Ramadoss, S. R. Ede, S. Kundu, *Nanoscale* **2014**, *6*, 8010; b) J. D. Xu, Q. M. Gao, Y. L. Zhang, Y. L. Tan, W. Q. Tian, L. H. Zhu, L. Jiang, *Sci. Rep.* **2014**, *4*, 1; c) S. Maitai, A. Pramanik, S. Mahanty, *ACS Appl. Mater. Interfaces* **2014**, *6*, 10754; d) F. Cao, G. X. Pan, X. H. Xia, P. S. Tang, H. F. Chen, *J. Power Sources* **2014**, *264*, 161; e) Y. Gao, Y. S. Zhou, M. Qian, X. N. He, J. Redepenning, P. Goodman, H. M. Li, L. Jiang, Y. F. Lu, *Carbon* **2013**, *51*, 52.

[6] a) J. Feng, X. Sun, C. Wu, L. Peng, C. Lin, S. Hu, J. Yang, Y. Xie, *J. Am. Chem. Soc.* **2011**, *133*, 17832; b) C. L. Zhang, H. H. Yin, M. Han, Z. H. Dai, H. Pang, Y. L. Zheng, Y. Q. Lan, J. C. Bao, J. M. Zhu, *ACS Nano* **2014**, *8*, 3761.

[7] J. M. Soon, K. P. Loh, *Electrochem. Solid-State Lett.* **2007**, *10*, A250.

[8] T. Brezesinski, J. Wang, S. H. Tolbert, B. Dunn, *Nat. Mater.* **2010**, *9*, 146.

[9] C. Wu, X. Lu, L. Peng, K. Xu, X. Peng, J. Huang, G. Yu, Y. Xie, *Nat. Commun.* **2013**, *4*, 1.

[10] L. Peng, X. Peng, B. Liu, C. Wu, Y. Xie, G. Yu, *Nano Lett.* **2013**, *13*, 2151.

[11] J. Xie, X. Sun, N. Zhang, K. Xu, M. Zhou, Y. Xie, *Nano Energy* **2013**, *2*, 65.

[12] X. Dong, L. Wang, D. Wang, C. Li, J. Jin, *Langmuir* **2012**, *28*, 293.

[13] Z. Zeng, Z. Yin, X. Huang, H. Li, Q. He, G. Lu, F. Boey, H. Zhang, *Angew. Chem. Int. Ed.* **2011**, *50*, 11093.

[14] K. G. Zhou, N. N. Mao, H. X. Wang, Y. Peng, H. L. Zhang, *Angew. Chem. Int. Ed.* **2011**, *50*, 10839.

[15] a) M. Lotya, Y. Hernandez, P. J. King, R. J. Smith, V. Nicolosi, L. S. Karlsson, F. M. Blighe, S. De, Z. Wang, I. T. McGovern, G. S. Duesberg, J. N. Coleman, *J. Am. Chem. Soc.* **2009**, *131*, 3611; b) V. Nicolosi, M. Chhowalla, M. G. Kanatzidis, M. S. Strano, J. N. Coleman, *Science* **2013**, *340*, 1; c) Y. Hernandez, V. Nicolosi, M. Lotya, F. M. Blighe, Z. Sun, S. De, I. T. McGovern, B. Holland, M. Byrne, Y. K. Gun'Ko, J. J. Boland, P. Niraj, G. Duesberg, S. Krishnamurthy, R. Goodhue, J. Hutchison, V. Scardaci, A. C. Ferrari, J. N. Coleman, *Nat. Nanotechnol.* **2008**, *3*, 563.

[16] P. May, U. Khan, A. O'Neill, J. N. Coleman, *J. Mater. Chem.* **2012**, *22*, 1278.

[17] a) Y. G. Yao, Z. Y. Lin, Z. Li, X. J. Song, K. S. Moon, C. P. Wong, *J. Mater. Chem.* **2012**, *22*, 13494; b) U. Khan, A. O'Neill, M. Lotya, S. De, J. N. Coleman, *Small* **2010**, *6*, 864; c) R. J. Smith, P. J. King, M. Lotya, C. Wirtz, U. Khan, S. De, A. O'Neill, G. S. Duesberg, J. C. Grunlan, G. Moriarty, J. Chen, J. Wang, A. I. Minett, V. Nicolosi, J. N. Coleman, *Adv. Mater.* **2011**, *23*, 3944; d) J. N. Coleman, M. Lotya, A. O'Neill, S. D. Bergin, P. J. King, U. Khan, K. Young, A. Gaucher, S. De, R. J. Smith, I. V. Shvets, S. K. Arora, G. Stanton, H. Y. Kim, K. Lee, G. T. Kim, G. S. Duesberg, T. Hallam, J. J. Boland, J. J. Wang, J. F. Donegan, J. C. Grunlan, G. Moriarty, A. Shmeliov, R. J. Nicholls, J. M. Perkins, E. M. Grieveson, K. Theuwissen, D. W. McComb, P. D. Nellist, V. Nicolosi, *Science* **2011**, *331*, 568; e) D. Hanlon, C. Backes, T. M. Higgins, M. Hughes, A. O'Neill, P. King, N. McEvoy, G. S. Duesberg, B. M. Sanchez, H. Pettersson, V. Nicolosi, J. N. Coleman, *Chem. Mater.* **2014**, *26*, 1751.

[18] J. F. Lambert, Z. Deng, J. B. d'Espinose, J. J. Fripiat, *J. Colloid Interface Sci.* **1989**, *132*, 337.

[19] M. S. Dresselhaus, A. Jorio, M. Hofmann, G. Dresselhaus, R. Saito, *Nano Lett.* **2010**, *10*, 751.

[20] H. Estrade-Szwarckopf, B. Rousseau, *J. Phys. Chem. Solids* **1992**, *53*, 419.

[21] a) Q. Mahmood, W. S. Kim, H. S. Park, *Nanoscale* **2012**, *4*, 7855; b) W. Tang, L. Liu, S. Tian, L. Li, Y. Yue, Y. Wu, K. Zhu, *Chem. Commun.* **2011**, *47*, 10058.

[22] a) X. Zhang, X. Zeng, M. Yang, Y. Qi, *ACS Appl. Mater. Interfaces* **2014**, *6*, 1125; b) J. Li, Q. M. Yang, I. Zhitomirsky, *J. Power Sources* **2008**, *185*, 1569; c) X. Xia, Q. Hao, W. Lei, W. Wang, H. Wang, X. Wang, *J. Mater. Chem.* **2012**, *22*, 8314.

[23] a) R. Liang, H. Cao, D. Qian, *Chem. Commun.* **2011**, *47*, 10305; b) L. Chen, L. J. Sun, F. Luan, Y. Liang, Y. Li, X. X. Liu, *J. Power Sources* **2010**, *195*, 3742.

[24] a) J. Li, X. Liu, *Mater. Lett.* **2013**, *112*, 39; b) I. Shakir, M. Shahid, S. Cherevko, C. H. Chung, D. J. Kang, *Electrochim. Acta* **2011**, *58*, 76; c) L. Zheng, Y. Xu, D. Jin, Y. Xie, *Chem. Asian J.* **2011**, *6*, 1505;

d) I. Shakir, M. Shahid, U. A. Rana, M. F. Warsi, *RSC Adv.* **2014**, *4*, 8741.
[25] Q. Mahmood, H. J. Yun, W. S. Kim, H. S. Park, *J. Power Sources* **2013**, *235*, 187.
[26] X. Lu, G. Wang, T. Zhai, M. Yu, J. Gan, Y. Tong, Y. Li, *Nano Lett.* **2012**, *12*, 1690.
[27] a) L. Y. Yuan, X. H. Lu, T. Zhai, J. J. Dai, F. H. Zhang, B. Hu, X. Wang, L. Gong, J. Chen, C. G. Hu, Y. X. Tong, J. Zhou, Z. L. Wang, *ACS Nano* **2011**, *6*, 656; b) P. S. P. L. Taberna, J. F. Fauvarque, *J. Electrochem. Soc.* **2003**, *150*, A292.
[28] a) S. K. Meher, G. R. Rao, *J. Phys. Chem. C* **2011**, *115*, 15646; b) S. K. Meher, P. Justin, G. R. Rao, *Nanoscale* **2011**, *3*, 683; c) P. Justin, S. K. Meher, G. R. Rao, *J. Phys. Chem. C* **2010**, *114*, 5203.
[29] Y. Jing, Q. Pan, Z. Cheng, X. Dong, Y. Xiang, *Mater. Sci. Eng., B* **2007**, *138*, 55.